Size-Selective Detection of Nanoparticles in Solution and Air by Imprinting

Linoy Dery,[#] Nitzan Shauloff,[#] Yury Turkulets, Ilan Shalish, Raz Jelinek,* and Daniel Mandler*

Cite This: *ACS Sens.* 2022, 7, 296−303

Read Online

ACCESS | Metrics & More | Article Recommendations | Supporting Information

ABSTRACT: Monitoring of nanoparticles (NPs) in air and aquatic environments is an unmet challenge accentuated by the rising exposure to anthropogenic or engineered NPs. The inherent heterogeneity in size, shape, and the stabilizing shell of NPs makes their selective recognition a daunting task. Thus far, only a few technologies have shown promise in detecting NPs; however, they are cumbersome, costly, and insensitive to the NPs morphology or composition. Herein, we apply an approach termed nanoparticle-imprinted matrices (NAIM), which is based on creating voids in a thin layer by imprinting NPs followed by their removal. The NAIM was formed on an interdigitated electrode (IDE) and used for the size-selective detection of silica NPs. Three- and 5-fold increases in capacitance were observed for the reuptake of NPs with similar diameter, compared to smaller or larger NPs, in air and liquid phase, respectively. En masse, the proposed approach lays the foundation for the emergence of field-effective, inexpensive, real-life applicable sensors that will allow online monitoring of NPs in air and liquids.

KEYWORDS: Nanoparticles detection, interdigitated electrode, imprinting, nanoparticle-imprinted matrices, aerosol, capacitive sensing
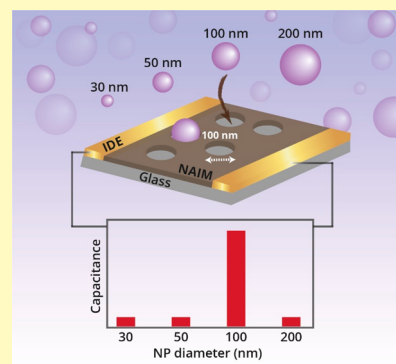
Human exposure to nanoparticles (NPs) is a growing concern due to the increased use of nanotechnology and nanomaterials in everyday life. Exposure to anthropogenic NPs is commonly divided[1−3] into processes, such as combustion,[4] that emit mostly carbonaceous NPs, and NP-based applications, e.g., painting and packaging.[5−8] The major health concern is undoubtedly the exposure to NPs from air.[9] Accordingly, the World Health Organization (WHO) has set regulations as to the exposure of humans to NPs in air.[10,11] Particulate matter (PM) is particles with dimensions of 0.1−10 μm, which are predominantly responsible for air pollution.[10] Numerous studies have shown that smaller NPs are considered more toxic due to their facile diffusion and penetration across tissues.[12−14] Therefore, PM was further categorized into $PM_{2.5}$ (0.1−2.5 μm) and $PM_{0.1}$ (<100 nm, known as ultrafine particles (UFP)) that are extremely dangerous.[10] These regulations have driven the development of monitoring technologies for NPs. The current techniques are either preweight sensors[15,16] or real-time optical counters[17,18] which are limited and usually cannot monitor UFPs. A recent report compared tens of portable air quality sensors all for PM_1−PM_{10} that are based on light scattering[19]

In this context, extensive research has been directed to the development of UFP sensors,[15,20] with several commercially available solutions.[15,21−29] However, these approaches are usually cumbersome, expensive, and insensitive to neither the structure and morphology nor the composition of the NPs.[20,30] There is currently no standardized method for the measurement or reporting of ambient UFPs, and therefore, no clear guidelines as to the acceptable levels.[31] Moreover, and to the best of our knowledge, there are currently no technologies for the continuous, real-time sensing and size discrimination of UFP in air, which are sensitive to the shape and, in particular, to the shell of engineered NPs. In this respect, the IUPAC recommendation of numerous techniques for NPs characterization should be mentioned, but these require heavy-duty instrumentation.[32] "Nanoparticle-imprinted matrices (NAIM)" is an innovative approach developed in our laboratory for NP sensing.[33−39] NAIM resembles the well-known molecularly imprinted polymer (MIP) approach.[40−43] In NAIM, nanocavities with specific size, shape, and chemical composition are formed through imprinting of NPs in soft thin layers.[33,35,37] The cavities can then reuptake NPs according to their size and surface properties. Notably, previous studies of NAIM systems were limited to metallic NPs and demonstrated applications only in solutions.

The purpose of this contribution is to demonstrate the feasibility of applying the NAIM concept to the detection of NPs in the gaseous phase. We hypothesize that the reuptake of particles by the imprinted nanovoid is not limited to solutions, and if properly designed, such matrices can transduce the recognition event into an electrical signal.
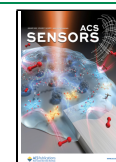
Accordingly, we present for the first time a capacitive-based NAIM system for size-selective recognition of NPs in air and solution. Capacitive sensors have been widely employed for monitoring volatile molecules or biological species via different thin films assembled on an interdigitated electrode (IDE),[44−46] The significant advantage of IDEs is their simple and low-cost mass production and the ability to easily modify them for different analytes.[47] Our design comprises the assembly of a NAIM layer on a commercially available IDE. The NAIM-IDE was formed by spin-coating of narrow-size-distributed latex NPs followed by filling the nonoccupied areas with a spin-coated sol−gel thin film. Subsequent thermal removal of the latex NPs resulted in imprinted nanocavities, which selectively recognized NPs from aerosol and solution by their size. A 3- and 5-fold increase in capacitance was observed upon exposure of a 100 nm imprinted NAIM-IDE to 100 nm silica NPs in air and solution, respectively, whereas other NPs having different sizes had almost no effect on the capacitance. These results emphasize the outstanding size-exclusion of the NAIM-IDE. The detection of the NPs is accomplished within short exposure (10 min) and, therefore, provides a promising platform for the fast and portable detection of NPs in air and solution.

■ RESULTS AND DISCUSSION

Fabrication of the NAIM-IDE. The experimental strategy for the detection of NPs in air and solution integrates the NAIM concept with capacitive sensing (Figure 1). In essence, narrow-size-distributed latex NPs are spin-coated on an IDE followed by spin-coating of a thin sol−gel film. After curing the latex, NPs are removed by thermal treatment to form the NPs imprinted matrix, i.e., NAIM-IDE. The reuptake, i.e., docking of NPs within the cavities, results in modulation of the matrix dielectric constant and a concomitant change in capacitance. This occurs since the IDE exhibits pronounced sensitivity toward changes in different surface properties of the capacitor medium. Specifically, the capacitance of the IDE sensor is defined by eq 1:

$$C = \eta \varepsilon_0 \varepsilon_r \frac{lt}{d} \tag{1}$$

in which C is the capacitance in Farads (F), η is the number of IDE fingers, ε_0 is the free space permittivity ($\varepsilon_0 = 8.854 \times 10^{-12}$ F/m), ε_r is the relative permittivity, commonly known as the dielectric constant. l and t are the lengths (or the distance between the electrodes) and thickness of the IDE, respectively, and d is the distance between the electrodes. The IDE displays an array of gold electrodes, in which the gaps between the electrodes can accommodate the NP recognition layer (Figure 1a). Importantly, the sensing layer is prepared through the NAIM methodology in which NPs are initially placed on the IDE and a thin film is formed covering the nonoccupied areas between the NPs. Removing the embedded NPs leaves behind cavities, which can reuptake the targeted NPs.[33−38]

The representative SEM images in Figure 1 correspond to a typical experiment in which latex NPs (100 nm diameter) are deposited on the IDE surface through spin-coating (Figure 1b). The conditions such as NP concentration and rotation speed (in rpm) for achieving a uniform dispersion were examined on a glass surface (Figure S1). Upon optimization, we found that a 0.25 wt % latex−NPs solution spin-coated at 3000 rpm resulted in a homogeneous distribution of the NPs, and is therefore used in all further experiments. A thin TEOS-
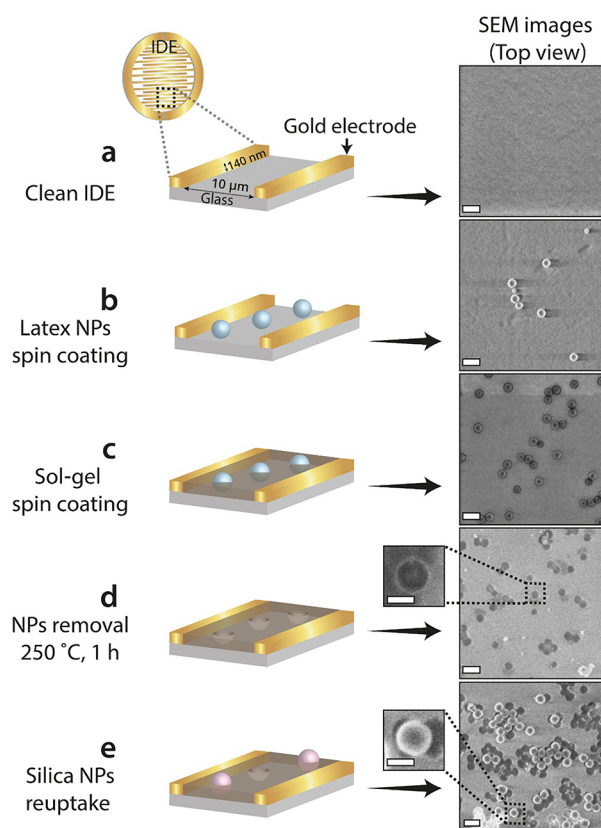

Figure 1. Schematic illustration of the NAIM-IDE-based approach (left) and the corresponding SEM images (right): (a) a bare IDE; (b) following spin-coated with latex-NPs; (c) upon spin-coated with sol−gel; (d) after removal of the latex NPs; (e) following the reuptake of 100 nm silica NPs. Scale bar: 200 nm.

based film was spin-coated on an IDE-latex surface (Figure 1c). The corresponding SEM image reveals that the TEOS film does not fully cover the NPs, which still protrude through the matrix. The spin-coating process of a thin sol−gel layer on the deposited latex NPs was examined and optimized to be approximately the size of the NP radius by changing the rotation speed or sol−gel solution concentration (Figures S2−3). It can be seen that at a low rotation speed (1500 rpm), the sol−gel layer covers the latex NPs (Figure S2a). Conversely, at 3000 rpm the sol−gel layer does not cover the NPs and forms a thin layer between them (Figures S2b and S3). Furthermore, Figure S4 shows the effect of the sol−gel concentration on the film that was formed. A TEOS layer is hardly seen for a 1:10 diluted sol−gel, whereas a thicker layer is formed as the concentration of the sol−gel increases.

Figure 1d shows the final step in which the latex NPs were removed by thermal decomposition (heating at 250 °C for 1 h) leaving behind voids with the size/shape of the NPs. This can also be seen in Figure S3 where the remaining voids after thermal treatment are more prominent as the sol−gel layer thickens. Notably, the TEOS layer was not affected by the heat treatment, and the SEM image in Figure 1d confirms the fidelity of the void sizes comparatively to the initially deposited NPs. A size compatibility analysis between the cavities and the latex NPs was conducted by measuring and comparing their diameter (Figure S5). This analysis shows excellent matching between the cavities that are formed by thermal treatment and the originally imprinted latex NPs. Notably, the advantage of

the two-step spin-coating preparation process of the NAIM-IDE is that the template (NPs) and host (TEOS matrix) are deposited separately, allowing, in principle, usage of various types of nanomaterial templates including biological species[48] and matrices for the imprinting process. Such flexibility cannot be accomplished with conventional one-step codeposition schemes.[49]

The presence of NPs modifies the ε_r which in turn changes the IDE capacitance. Figure S6 shows the capacitance signal at different stages. An increase in the capacitance is observed following spin-coating of latex NPs and a TEOS layer, whereas a decrease in capacitance is observed after the removal of the latex NPs. These results confirm that the capacitive signal is sensitive to the different stages and confirm that silica NPs reuptake leads to an increase in capacitance. The capacitance increases as the silica NPs accommodate the empty voids, since ε_r of the empty cavities is considerably lower than that of the surrounding sol−gel matrix.[50,51] Yet, the most striking results are the size-selectivity of the matrix toward silica NPs and the corresponding capacitance measurements, *vide infra*.

Size-Selective NP Detection in Solution. Figure 2 shows the normalized change in capacitance for NAIM-IDE
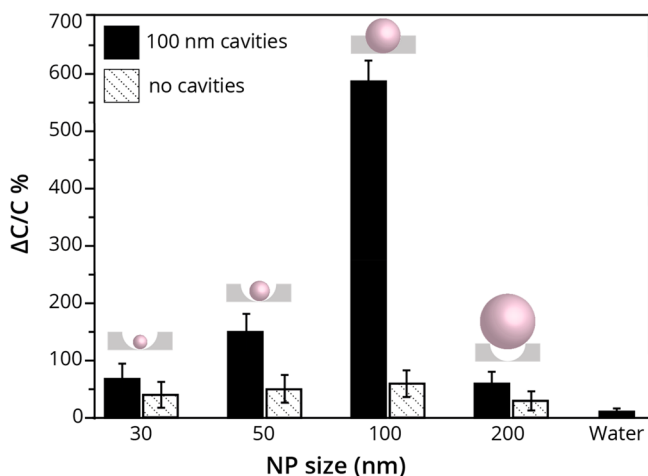

Figure 2. Normalized capacitance change upon the reuptake of variable silica diameter NPs from solution (30, 50, 100, and 200 nm) using NAIM-IDE imprinted by 100-nm-diameter latex NPs (black columns) and by nonimprinted IDE-TEOS (dotted columns).

and IDE-TEOS after re-uptaking silica NPs of different diameters. Specifically, the normalized difference (the difference divided by the initial value) in capacitance is measured for a nonimprinted IDE that was spin-coated with TEOS (dotted columns), after exposure for 10 min to solutions of different diameter NPs (1 mg/mL concentration). The measurements were performed after the IDEs were removed from the silica NP solution and dried. A slight increase of the capacitance (<50%) implies that some silica NPs are nonspecifically adsorbed on top of the sol−gel film. On the other hand, a significant increase in the capacitance is observed upon exposing the NAIM-IDE (after removal of the latex-NPs) to silica NPs (black columns). Yet, the increase varies dramatically depending on the NP diameter. We recall that the NAIM-IDE was imprinted by 100-nm-diameter latex NPs, which created voids in a similar shape. The most significant capacitance increase is detected when the NAIM-IDE is immersed in a 100 nm silica NPs solution. Notably, NAIM-

IDE that were immersed in solutions containing silica NPs bearing different diameters (30, 50, and 200 nm) resulted in a slight capacitance increase. Overall, the capacitive response data in Figure 2 confirm that the reuptake of NPs within the imprinted surface likely constitutes the proposed signal transduction mechanism. Moreover, the matching between the NP and cavity size, i.e., cavity diameter, plays a critical role in signal generation and facilitated size exclusion. Similarly, the change in capacitance due to the reuptake of silica NPs is affected by the size of the NPs and their surface concentration. For instance, the accommodation of a void by a smaller NP will have a smaller impact on the capacitance. Finally, the amount of water that can interact with the silica NPs also has an effect on ε_r, causing an increase in the total capacitance. The match between the NP size and the voids is also seen by comparing the size distribution of the different NP populations and the imprinted voids (Figure S7). The SEM images show silicon surfaces on which the various NPs were adsorbed and size analyzed as shown below the SEM images. Evidently, there is an excellent match between the size distribution of the 100 nm silica NPs and that of the 100 nm latex-imprinted voids.

Additional SEM images of NAIM-IDE surfaces bearing 100-nm-sized cavities following exposure to 30-, 50-, and 100-nm-sized silica NPs (Figure 3a (I−III)) visually illustrate the size-
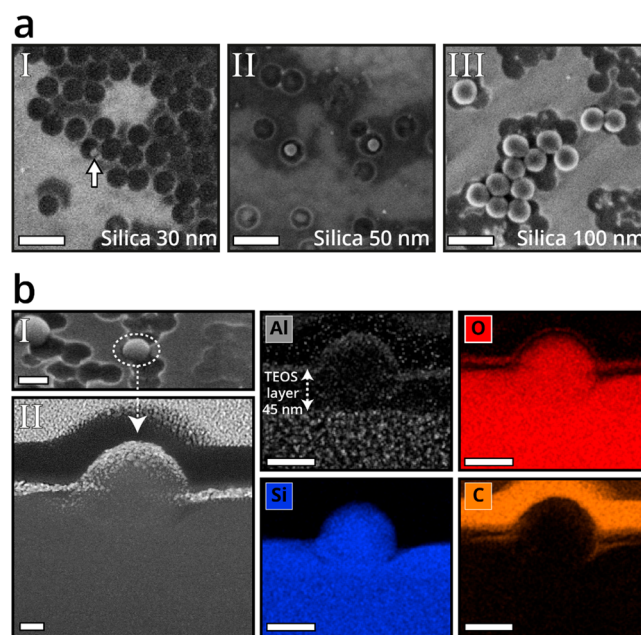

Figure 3. (a) SEM images of a 100 nm imprinted NAIM-IDE after reuptake of silica NPs: 30, 50, and 100 nm (I−III, respectively). Scale bar: 200 nm. (b) SEM and STEM-HAADF/EDS images of a NAIM-IDE system following the reuptake process of silica NPs. (I) SEM image of a 100 nm silica NPs inside a cavity (taken with a tilting angle of 52°). (II) STEM-HAADF image of a lamellar cross-section containing the same NP in (I) performed by focused-ion beam. Elemental mapping of Al, O, Si, and C of silica NPs lamella. Scale bar: 100 (A−I), 20 (B−I), and 50 nm.

selective NP reuptake. A small minority of cavities appear occupied upon exposure to 30 or 50 nm silica NPs, and remarkably, reuptake of multiple NPs inside a large cavity is not observed. This phenomenon is attributed to a statistical effect along with a relatively weak interaction between small NPs and a larger cavity. It is hypothesized that the strong

interaction between NP and a matching void (Figure 3a III) surpasses the repulsion forces that are expected between NPs, enabling them to accommodate even in contacting cavities.

Complementary high-resolution SEM and TEM characterizations were performed (Figure 3b) to disclose the intimate contact between the NP and the void. Focused-ion beam (FIB) was used to slice the NAIM-IDE through a single 100 nm NP accommodated inside a cavity. The NP and the layer are covered by Pt and carbon to protect them while slicing the lamella. Notably, while the exposed part of the NP is evident, the interface between the NP and the sol−gel layer can hardly be seen. The reason for that is that they are made of the same material and are therefore indistinguishable by the e-beam. Yet, this also implies that there is close contact between the two, which means that the NP fits extremely well inside the void. Elemental analysis of the lamellar cross-section confirms that, indeed, the NP is composed of SiO_2 indicating that this particle was captured in the reuptake process rather than a latex-NP left on the surface from the preparation stage (Figure 3b-Si/O/C). Importantly, the Al elemental imaging reveals that the thickness of the TEOS recognition layer is ca. 45 nm, which fits well with the mean size of the NP radius (Figures 3b-Al and S4). We have shown that the highest reuptake percentage is achieved when the NAIM thickness is approximately equal to the NP radius, because it provides an optimized interacting area, and at the same time, it allows NPs to ingress and egress the cavity.[33] It is assumed that the seamless matching and close contact between the NPs and the matrix will result in a maximum capacitance change.[52]

We believe that the source of the high size-selectivity lies in physical as well as chemical matching. On one hand, physical forces of the cavity sidewalls that physically catch better NPs of an identical size than smaller NPs that have lower surface interaction with the cavity (less physical matching). On the other hand, the chemical interaction between the matrix and the NPs also plays an important role. The matrix is prepared of a TEOS precursor, whereas the NPs are made of SiO_2. The sol−gel layer contains hydroxyl groups (Si−OH), Si−O−Si, or Si−O−CH_3−CH_3 that can interact with the silica NPs surface, which contains similar hydroxyl groups (Si−OH) or Si−O−Si bonds. Therefore, hydrogen bonding is the leading non-covalent interaction, that is responsible also for the high selectivity. Additionally, the IDE surface is made of glass, which can contribute to hydrogen bonding with the SiO_2 NPs.

Size-Selective NP Detection in Air. Yet, and as mentioned above, it is by far more important to develop such detection capabilities for engineered NPs in the air. Combating UFP is only in the beginning and lacks appropriate tools. The application of the NAIM-IDE sensor for size-exclusion detection of NPs in the air is presented in Figure 4. The experimental setup (Figure 4a) comprises aerosolized silica NPs generated by a pressurized air-flow pipe connected to a jet-nebulizer containing diluted NP solutions. NAIM-IDE electrodes (imprinted with 100 nm latex NPs) were exposed to the NPs aerosol and flushed subsequently with dry N_2 prior to capacitance measurements. In the experiment, the capacitance of a NAIM-IDE bearing 100 nm cavities was measured following 15 min exposure to aerosolized silica NPs with different diameters. As an important control, the capacitance of nonimprinted TEOS-IDEs was measured following an identical treatment. Remarkably, an almost 3-fold higher capacitive signal was recorded for the aerosol containing 100 nm silica NPs as compared with aerosols of other NP sizes. The bar
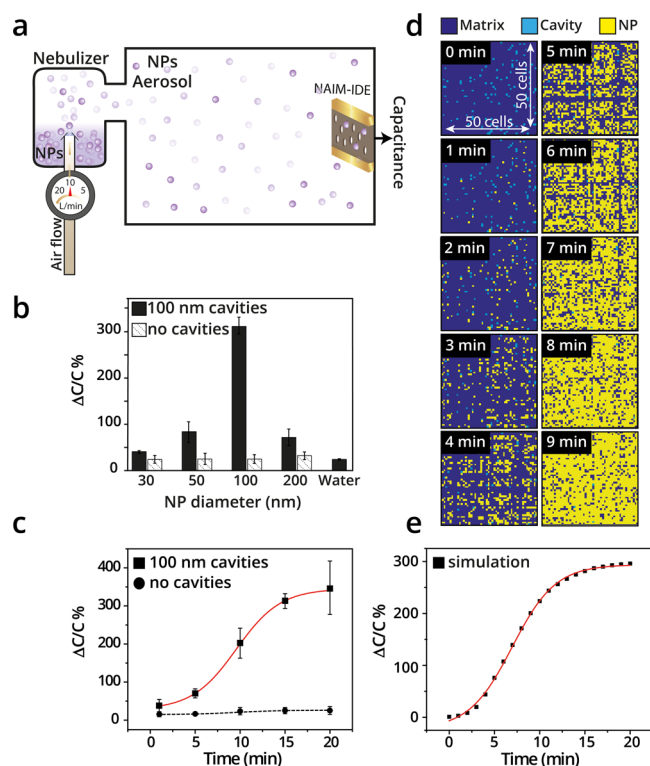

Figure 4. (a) Schematic illustration of the NPs-aerosol apparatus used for the NPs detection in air. (b) Normalized capacitance change following 15 min exposure to variable silica NP diameter aerosols (30, 50, 100, and 200 nm), using 100-nm-diameter imprinted cavities (black columns) and nonimprinted TEOS-IDE (dashed columns). (c) Normalized capacitance change of NAIM-IDE (square symbols) and TEOS-IDE (circle symbols), following exposure to 100 nm silica NPs aerosol recorded for different exposure times. (the red line represents a sigmoidal fitting with R^2 equals 0.999). (d) Schematic representation of the mathematical model describing the exposure of NAIM-IDE to NPs aerosol at different time points. Each time point consists of 50 × 50 color-coded cells: dark blue - sol−gel matrix; light blue - empty cavities (air); and yellow - silica NPs. (e) Calculated capacitance values upon exposure of the NAIM-IDE to silica NPs aerosol for different time points (the red line represents a sigmoidal fitting with R^2 equals 0.998).

diagram in Figure 4b summarizes the obtained capacitance values and highlights the excellent size selectivity of the NAIM-IDE ensuing its exposure to vaporized NPs. This result confirms the feasibility of utilizing the NAIM-IDE for size-selective detection of NPs in the air as well. Comparison between the size-selectivity results for solution and air demonstrates a similar trend for both phases. The highest capacitance change is observed for 100 nm silica NPs, whereas an insignificant change in capacitance is observed for smaller or larger NPs, comparable to the blank measurement signal. These results show that the size-selectivity characteristic of our sensor is phase-independent.

Figure 4c shows the change in the normalized capacitance as a function of exposure time to 100-nm-diameter aerosolized silica NPs, for the imprinted and nonimprinted samples. It should be noted that the concentration of the NPs in the aerosol is likely to play a similar role such as the time of exposure. Yet, it requires a better monitoring system, and therefore, we developed our approach and simulation for the time domain. The difference between the normalized capacitance values is outstanding, ranging from 5- to 30-fold

higher capacitance for the imprinted NAIM-IDE. A noticeable capacitance change was observed already after 5 min indicating the sensitivity of the NAIM-IDE that requires only short exposure times to produce a decent signal. In contrast, the time-dependent capacitance signal attained for the blank measurements shows a negligible increase in capacitance over time. This means that the nonspecific adsorption of silica NPs on top of the matrix or inside defects hardly affects the capacitance signal. The obtained capacitance values follow a sigmoidal trend, which can be explained by a percolation theory. In essence, this theory describes the onset creation of a network that at a critical fraction of formation (percolation threshold, manifested as the deflection point) forms large clusters that lead to a dramatic leap in the signal.

To interpret the observed sigmoidal capacitance trend, a simulation of the NAIM-IDE detection was performed by random filling of cavities in a square mesh grid that represents the area between the IDE "fingers", as illustrated in Figure 4d. In the simulated model, the capacitance of the cavities changes in the case of reuptake events as follows: (i) for a single reuptake event the capacitance changes linearly; (ii) reuptake events occur in clusters, in which the filled cavities are adjacent to each other, lead to a nonlinear correlation, i.e., a steeper increase in the capacitance. This occurs since the empty cavities that are located between or in the vicinity of a cluster are also considered as filled, due to their shielded electric field.[53] Therefore, the percolation threshold, which is the deflection point in the simulated model, illustrates the specific time point in which reuptake of silica NPs forms clusters in the NAIM.

Figure 4d shows 10 time shots during the simulation depicting the reuptake of silica NPs by the surface cavities. Each shot shows an array of 50 by 50 cells. The color of each cell represents the value of its dielectric constant: dark blue corresponds to the sol−gel matrix, light blue to unoccupied cavities, and yellow to a silica NP. As a visual aid, we converted the sequence of plots of Figure 4d to a GIF animation (Figure S8). Initially, the array consists of a sol−gel matrix bearing a finite number of air cavities. Following the first iteration, some of these cavities are filled by silica NPs. In the next time frames, more cavities are filled, and clusters of silica NPs are formed until all the cavities are covered.

Importantly, the simulated capacitance curve features a sigmoidal shape (Figure 4e) which is very similar to the observed experimental curve. This sigmoidal shape can be explained by the percolation mechanism, in which at short exposure times the capacitance increases linearly as the signal is correlated with isolated reuptake events. Upon longer exposure times, the capacitance increases significantly in a nonlinear manner. At a specific time point, called the percolation threshold, clusters of reuptaken silica NPs start to form, and the capacitance is affected also by occupied adjacent cavities. Finally, the capacitance signal exhibits only a slight increase because the added silica NPs join existing clusters and do not form new clusters. SEM-based analysis conducted on the samples exposed to the aerosolized silica NPs for different times shows a linear dependence (Figure S9) indicating that the rate of reuptake is constant. The fact that the capacitance change is sigmoidal implies that there must be a mechanism such as clustering to account for the nonlinear contribution of the reuptake process. Importantly, this result shows that the maximal signal is achieved via filling of only 10% of the cavities

by silica NPs, illustrating that the NAIM-IDE system is highly sensitive to the NPs reuptake.

■ CONCLUSIONS

This work demonstrates for the first time the selective detection of NPs in air and liquids using an imprinting approach. The combination of the nanoparticle-imprinted matrices (NAIM) concept with a transducer, which is an interdigitated electrode (IDE), resulted in a unique sensing platform. The NAIM-IDE was formed by spin-coating monosized NPs on an IDE followed by the formation of a thin sol−gel layer by spin-coating and the subsequent NP removal by thermal treatment. It should be noted that in this preliminary work the imprinting and reuptake were not carried out with the same NPs. While latex NPs were used for the imprinting, reuptake was examined on the same size of NPs, however, made of silica. This was reasoned by the ease of the thermal removal of the latex NPs. Yet, it is also important to take into account the chemical interactions in addition to the physical, i.e., structural considerations. This will allow a substantial increase in the selectivity. The voids that were formed served as size-selective binding sites for silica NPs. Reuptake events are then followed by changes in the capacitance of the NAIM-IDE. Solution-phase sensing was demonstrated using a wide size range of silica NPs, highlighting the excellent selectivity of the system following relatively short exposure times. Size-selective NPs detection in aerosol was demonstrated experimentally and theoretically. The experimental and simulated capacitance behavior followed a sigmoidal dependence with exposure time, a trend that was explained by the percolation theory. The developed NAIM-IDE approach paves the way for simple, rapid, and cost-effective selective detection of NPs to microparticles, such as nanoplastics and carbon that are found in aquatic systems and the air.

■ EXPERIMENTAL SECTION

Materials. Tetraethyl orthosilicate (TEOS, 98%, Sigma-Aldrich), silica NPs (10 mg/mL, in water) with a mean diameter of 30, 50, 100, and 200 nm and size distribution ≤12%, were ordered from nanoComposix (San Diego, CA, USA). Thin-film gold interdigitated electrodes (IDEs) 10/10 μm electrode/gap were obtained from Micrux (Gijón (Asturias), Spain). Latex nanoparticles stabilized with sodium dodecyl sulfate (100 mg/mL, in water) were purchased from Bangs Laboratories, Inc. (Fishers, IN, USA). Ultrapure water (EasyPure UV, Barnstead 18.3 MΩ cm) was used for all the experiments. All other chemicals were purchased from Sigma-Aldrich and used as received.

Characterization. Extra-high-resolution scanning electron microscopy (XHR-SEM, Magellan XHR 400L, FEI) was used applying a low voltage electron beam of 2 kV. High-resolution, high-angle annular dark-field (HAADF) scanning transmission electron microscopy (STEM) images and elemental mapping were acquired with a FEI Themis G3 at 300 keV instrument. Focused-ion beam (FIB, 460F1 Dual Beam, FEI Helios Nano Lab) was employed to slice lamellas from the IDE-NAIMs. A spin-coater (WS-400A-6NPP, Laurell, North Wales, PA, USA) was used for spin-coating of latex NPs and TEOS. Capacitance values were recorded using an LCR meter (Keysight Technologies, E4980AL Precision LCR Meter). A standard humidity sensor (TH 210, KIMO, Instruments, France) was used for monitoring the relative humidity.

Sol−Gel Preparation. 7 mL ethanol, 1 mL water, and 30 μL 95% HNO$_3$ were stirred for 1 min at 400 rpm. Then, 1.1 mL of TEOS was added, and the vessel was heated to 40 °C and mixed for 1 h. The

resulting solution was allowed to cool to room temperature and used immediately.

Sample Preparation. IDEs were cleaned with ethanol. After drying, 20 μL of 0.25 wt % 100 nm latex spheres solution were deposited on the IDE and spin-coated for 1 min at 3000 rpm with an acceleration of 1290 rpm/s. The IDE-latex was dried at 65 °C for 30 min, after cooling, 5 μL of prepared TEOS solution was deposited on the IDE-latex and spin-coated for 1 min at 3000 rpm with an acceleration of 1290 rpm/s. The IDE-latex-TEOS was dried at room temperature overnight. Finally, the latex NPs were removed by thermal treatment of the IDE-latex-TEOS at 250 °C for 1 h to form the IDE-NAIM.

Capacitance Measurements. The initial capacitance for each electrode, IDE-TEOS or IDE-NAIM, was measured after 30 min of nitrogen purging at 50% relative humidity (RH) and frequency of 1000 Hz. Then, the modified IDEs were placed in a diluted solution (1 mg/mL) of silica NPs (30, 50, 100, or 200 nm) for 10 min during stirring with a magnetic stirrer. The modified IDEs were removed, washed with N_2 gas flow, and kept under vacuum overnight. The capacitance of the modified IDEs was measured exactly as mentioned above. The change in capacitance was calculated using the formula $(\Delta C/C)\%$; where ΔC refers to the change between the capacitance after reuptake and the initial capacitence, C. The reuptake of silica NPs from the gas phase was measured by placing the IDE-NAIM or IDE-TEOS in a $15 \times 8 \times 12$ cm^3 PMMA box to which NP-aerosol was pumped through a nebulizer using a diluted solution (0.2 mg/mL) of silica-NPs (50, 100, or 200 nm) under a constant air flow of 10 L/min.

Simulation. The simulation was carried out using Matlab. To simulate the dielectric material between the capacitor fingers, we used an array of cells. The value of each cell in the array represented the dielectric constant, which was initially set to be equal to the dielectric constant of the sol−gel. Part of the cells in the array were then defined to be cavities, having the dielectric constant of air. The total number of cavities was defined by a simulation parameter as a percentage from the total number of cells in the array. To simulate the operation of jet-nebulizer, we used a generator of random numbers operating in a loop. At each iteration, the generator randomly provided a series of numbers. The value of each number was compared with indices of cells in the array. If one or more of the generated numbers were found equal to indices of cells representing cavities, the dielectric constant of the corresponding cell would be replaced by that of silica. This way, the reuptake of silica nanoparticles by a NAIM was simulated. To simulate an agglomeration of silica particles, we added an additional term: if the generated random number was equal to a cell number located in immediate proximity to a cell already occupied by a silica particle, its value could also be replaced by the value of silica with a certain probability defined as another simulation parameter. At the end of each iteration, we calculated the change in the capacitance with respect to the initial capacitance of the structure. The above process was then repeated with a finite number of iterations. The simulation was carried out for 20 min (that equals 21 iterations).

ASSOCIATED CONTENT

Ⓢ Supporting Information

The Supporting Information is available free of charge at https://pubs.acs.org/doi/10.1021/acssensors.1c02324.

Brief description of contents: SEM images of the spin-coating process of latex NPs and sol−gel on glass. STEM-HAADF image of a lamellar cross-section containing latex NPs. Histograms of latex NPs, silica NPs, and cavities. The capacitance value of the different stages for the NAIM-IDE formation and sensing. A GIF animation showing the simulation. SiO$_2$ NPs reuptake, divided by the average number of cavities. (PDF)

AUTHOR INFORMATION

Corresponding Authors

Daniel Mandler − *Institute of Chemistry, the Hebrew University of Jerusalem, Jerusalem 9190401, Israel;* ⓘ orcid.org/0000-0003-2490-1084; Email: Daniel.mandler@mail.huji.ac.il

Raz Jelinek − *Ilse Katz Institute for Nanotechnology, Ben Gurion University of the Negev, Beer Sheva 8410501, Israel;* ⓘ orcid.org/0000-0002-0336-1384; Email: razj@bgu.ac.il

Authors

Linoy Dery − *Institute of Chemistry, the Hebrew University of Jerusalem, Jerusalem 9190401, Israel*

Nitzan Shauloff − *Ilse Katz Institute for Nanotechnology, Ben Gurion University of the Negev, Beer Sheva 8410501, Israel*

Yury Turkulets − *School of Electrical Engineering, Ben-Gurion University, Beer Sheva 8410501, Israel*

Ilan Shalish − *School of Electrical Engineering, Ben-Gurion University, Beer Sheva 8410501, Israel*

Complete contact information is available at:
https://pubs.acs.org/10.1021/acssensors.1c02324

Author Contributions

[#]L.D. and N.S. contributed equally.

Notes
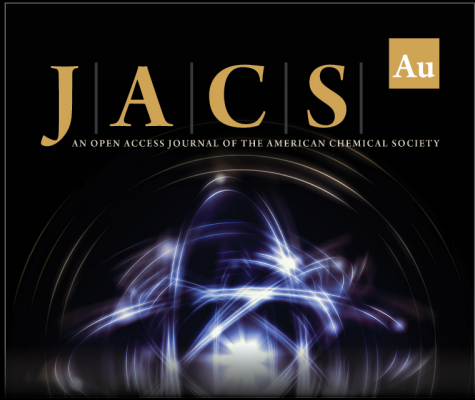
The authors declare no competing financial interest.

REFERENCES

(1) Lespes, G.; Faucher, S.; Slaveykova, V. I. Natural Nanoparticles, Anthropogenic Nanoparticles, Where Is the Frontier? *Frontiers in Environmental Science* **2020**, *8*, 71.

(2) Sadik, O. A. Anthropogenic nanoparticles in the environment. *Environmental Science: Processes & Impacts* **2013**, *15* (1), 19−20.

(3) Trejos, E. M.; Silva, L. F.; Hower, J. C.; Flores, E. M.; González, C. M.; Pachón, J. E.; Aristizábal, B. H. Volcanic emissions and atmospheric pollution: A study of nanoparticles. *Geoscience Frontiers* **2021**, *12* (2), 746−755.

(4) D'Anna, A. Combustion-formed nanoparticles. *Proceedings of the Combustion Institute* **2009**, *32* (1), 593−613.

(5) El-Feky, O. M.; Hassan, E. A.; Fadel, S. M.; Hassan, M. L. Use of ZnO nanoparticles for protecting oil paintings on paper support against dirt, fungal attack, and UV aging. *Journal of Cultural Heritage* **2014**, *15* (2), 165−172.

(6) Espitia, P.; Otoni, C.; Soares, N. Zinc oxide nanoparticles for food packaging applications. In *Antimicrobial food packaging*; Elsevier: 2016; pp 425−431.

(7) Espitia, P. J. P.; Soares, N. d. F. F.; dos Reis Coimbra, J. S.; de Andrade, N. J.; Cruz, R. S.; Medeiros, E. A. A. Zinc oxide nanoparticles: synthesis, antimicrobial activity and food packaging applications. *Food and bioprocess technology* **2012**, *5* (5), 1447−1464.

(8) Souza, V. G. L.; Fernando, A. L. Nanoparticles in food packaging: Biodegradability and potential migration to food—A review. *Food Packaging and Shelf Life* **2016**, *8*, 63−70.

(9) Card, J. W.; Zeldin, D. C.; Bonner, J. C.; Nestmann, E. R. Pulmonary applications and toxicity of engineered nanoparticles. *American Journal of Physiology-Lung Cellular and Molecular Physiology* **2008**, *295* (3), L400−L411.

(10) https://www.who.int/, last accessed date: 6/12/2021.

(11) https://www.epa.gov/, last accessed date: 6/12/2021.

(12) Kik, K.; Bukowska, B.; Sicińska, P. Polystyrene nanoparticles: sources, occurrence in the environment, distribution in tissues, accumulation and toxicity to various organisms. *Environ. Pollut.* **2020**, *262*, 114297.

(13) Sengul, A. B.; Asmatulu, E. Toxicity of metal and metal oxide nanoparticles: a review. *Environmental Chemistry Letters* **2020**, *18*, 1659.

(14) Sokolova, V.; Nzou, G.; van der Meer, S. B.; Ruks, T.; Heggen, M.; Loza, K.; Hagemann, N.; Murke, F.; Giebel, B.; Hermann, D. M. Ultrasmall gold nanoparticles (2 nm) can penetrate and enter cell nuclei in an in vitro 3D brain spheroid model. *Acta biomaterialia* **2020**, *111*, 349−362.

(15) Rezaei, M.; Johnson, M. S. *Airborne Nanoparticles: Control and Detection.* **2021**, 85−133.

(16) Ghio, A. J.; Huang, Y.-C. T. Exposure to concentrated ambient particles (CAPs): a review. *Inhalation toxicology* **2004**, *16* (1), 53−59.

(17) Horender, S.; Auderset, K.; Vasilatou, K. Facility for calibration of optical and condensation particle counters based on a turbulent aerosol mixing tube and a reference optical particle counter. *Rev. Sci. Instrum.* **2019**, *90* (7), 075111.

(18) Szymanski, W.; Liu, B. Y. On the sizing accuracy of laser optical particle counters. *Particle & particle systems characterization* **1986**, *3* (1), 1−7.

(19) http://www.aqmd.gov/aq-spec/evaluations/summary-pm, last accessed date: 6/12/2021.

(20) Nizamov, S.; Kasian, O.; Mirsky, V. M. Individual detection and electrochemically assisted identification of adsorbed nanoparticles by using surface plasmon microscopy. *Angew. Chem., Int. Ed.* **2016**, *55* (25), 7247−7251.

(21) Kulkarni, P.; Baron, P. A.; Willeke, K. *Aerosol measurement: principles, techniques, and applications*; John Wiley & Sons, 2011.

(22) Malloy, Q. G.; Nakao, S.; Qi, L.; Austin, R.; Stothers, C.; Hagino, H.; Cocker, D. R., III Real-time aerosol density determination utilizing a modified scanning mobility particle sizer—aerosol particle mass analyzer system. *Aerosol Sci. Technol.* **2009**, *43* (7), 673−678.

(23) Xu, R. *Light scattering: A review of particle characterization applications.* **2015**, *18*, 11−21.

(24) Bauer, P.; Amenitsch, H.; Baumgartner, B.; Köberl, G.; Rentenberger, C.; Winkler, P. In-situ aerosol nanoparticle characterization by small angle X-ray scattering at ultra-low volume fraction. *Nat. Commun.* **2019**, *10* (1), 1−7.

(25) Stolzenburg, M. R.; McMurry, P. H. An ultrafine aerosol condensation nucleus counter. *Aerosol Sci. Technol.* **1991**, *14* (1), 48−65.

(26) Knutson, E.; Whitby, K. Aerosol classification by electric mobility: apparatus, theory, and applications. *J. Aerosol Sci.* **1975**, *6* (6), 443−451.

(27) Wang, S. C.; Flagan, R. C. *Scanning electrical mobility spectrometer.* **1990**, *13*, 230−240.

(28) Wang, Y.; Pinterich, T.; Wang, J. Rapid measurement of sub-micrometer aerosol size distribution using a fast integrated mobility spectrometer. *J. Aerosol Sci.* **2018**, *121*, 12−20.

(29) Tröstl, J.; Tritscher, T.; Bischof, O. F.; Horn, H.-G.; Krinke, T.; Baltensperger, U.; Gysel, M. Fast and precise measurement in the sub-20 nm size range using a Scanning Mobility Particle Sizer. *J. Aerosol Sci.* **2015**, *87*, 75−87.

(30) Liu, X.; Chen, X.; Chen, T.; Xu, Y.; Zeng, X. Time-Resolved Selective Electrochemical Sensing of Carbon Particles. *Anal. Chem.* **2021**, *93*, 761.

(31) Kwon, H.-S.; Ryu, M. H.; Carlsten, C. Ultrafine particles: unique physicochemical properties relevant to health and disease. *Experimental & molecular medicine* **2020**, *52* (3), 318−328.

(32) Gubala, V.; Johnston, L. J.; Liu, Z.; Krug, H.; Moore, C. J.; Ober, C. K.; Schwenk, M.; Vert, M. Engineered nanomaterials and human health: Part 1. Preparation, functionalization and character-ization (IUPAC Technical Report). *Pure Appl. Chem.* **2018**, *90* (8), 1283−1324.

(33) Bruchiel-Spanier, N.; Dery, L.; Tal, N.; Dery, S.; Gross, E.; Mandler, D. Effect of matrix-nanoparticle interactions on recognition of aryldiazonium nanoparticle-imprinted matrices. *Nano Research* **2019**, *12* (2), 265−271.

(34) Bruchiel-Spanier, N.; Giordano, G.; Vakahi, A.; Guglielmi, M.; Mandler, D. Electrochemically Deposited Sol−Gel Based Nano-particle-Imprinted Matrices for the Size-Selective Detection of Gold Nanoparticles. *ACS Applied Nano Materials* **2018**, *1* (10), 5612−5619.

(35) Bruchiel-Spanier, N.; Mandler, D. Nanoparticle-Imprinted Polymers: Shell-Selective Recognition of Au Nanoparticles by Imprinting Using the Langmuir−Blodgett Method. *ChemElectroChem.* **2015**, *2* (6), 795−802.

(36) Hitrik, M.; Pisman, Y.; Wittstock, G.; Mandler, D. Speciation of nanoscale objects by nanoparticle imprinted matrices. *Nanoscale* **2016**, *8* (29), 13934−13943.

(37) Kraus-Ophir, S.; Witt, J.; Wittstock, G.; Mandler, D. Nanoparticle-Imprinted Polymers for Size-Selective Recognition of Nanoparticles. *Angew. Chem., Int. Ed.* **2014**, *53* (1), 294−298.

(38) Witt, J.; Mandler, D.; Wittstock, G. Nanoparticle-Imprinted Matrices as Sensing Layers for Size-Selective Recognition of Silver Nanoparticles. *ChemElectroChem.* **2016**, *3* (12), 2116−2124.

(39) Zelikovich, D.; Dery, S.; Bruchiel-Spanier, N.; Tal, N.; Savchenko, P.; Gross, E.; Mandler, D. Shell−Matrix Interaction in Nanoparticle-Imprinted Matrices: Implications for Selective Nano-particle Detection and Separation. *ACS Applied Nano Materials* **2021**, *4*, 10819.

(40) Haupt, K. Molecularly imprinted polymers in analytical chemistry. *Analyst* **2001**, *126* (6), 747−756.

(41) Pichon, V.; Chapuis-Hugon, F. Role of molecularly imprinted polymers for selective determination of environmental pollutants—a review. *Anal. Chim. Acta* **2008**, *622* (1−2), 48−61.

(42) Tokonami, S.; Shiigi, H.; Nagaoka, T. Micro-and nanosized molecularly imprinted polymers for high-throughput analytical applications. *Analytica chimica acta* **2009**, *641* (1−2), 7−13.

(43) Whitcombe, M. J.; Kirsch, N.; Nicholls, I. A. Molecular imprinting science and technology: a survey of the literature for the years 2004−2011. *Journal of Molecular Recognition* **2014**, *27* (6), 297−401.

(44) Shauloff, N.; Teradal, N. L.; Jelinek, R. Porous Graphene Oxide−Metal Ion Composite for Selective Sensing of Organo-phosphate Gases. *ACS sensors* **2020**, *5* (6), 1573−1581.

(45) Rao, V. K.; Teradal, N. L.; Jelinek, R. Polydiacetylene capacitive artificial nose. *ACS Appl. Mater. Interfaces* **2019**, *11* (4), 4470−4479.

(46) Staginus, J.; Aerts, I. M.; Chang, Z.-y.; Meijer, G. C.; de Smet, L. C.; Sudhölter, E. J. Capacitive response of PDMS-coated IDE platforms directly exposed to aqueous solutions containing volatile organic compounds. *Sens. Actuators, B* **2013**, *184*, 130−142.

(47) Venkatesh, M. R.; Sachdeva, S.; El Mansouri, B.; Wei, J.; Bossche, A.; Bosma, D.; de Smet, L. C.; Sudhölter, E. J.; Zhang, G. Q. A low-power MEMS IDE capacitor with integrated microhotplate: application as methanol sensor using a metal-organic framework coating as affinity layer. *Sensors* **2019**, *19* (4), 888.

(48) Bräuer, B.; Unger, C.; Werner, M.; Lieberzeit, P. A. Biomimetic Sensors to Detect Bioanalytes in Real-Life Samples Using Molecularly Imprinted Polymers: A Review. *Sensors* **2021**, *21* (16), 5550.

(49) Li-Destri, G.; Tummino, A.; Gasperini, A. M.; Monreal, L. P.; Messina, G.; Spampinato, V.; Ceccone, G.; Konovalov, O. Filling nanoporous polymer thin films: an easy route toward the full control of the 3D nanostructure. *RSC Adv.* **2016**, *6* (11), 9175−9179.

(50) Rodríguez-Serna, J. M.; Albarracín-Sánchez, R. Numerical simulation of temperature and pressure changes due to partial discharges in spherical cavities within solid dielectrics at different ageing conditions. *Energies* **2019**, *12* (24), 4771.

(51) Wang, Y.-T.; Hu, Y.-C.; Chu, W.-C.; Chang, P.-Z. The fringe-capacitance of etching holes for CMOS-MEMS. *Micromachines* **2015**, *6* (11), 1617−1628.

(52) Lee, H.; Baeg, S.; Hua, N.; Wen, S. Temporal and frequency characteristic analysis of margin-related failures caused by an intermittent nano-scale fracture of the solder ball in a BGA package device. *Microelectronics Reliability* **2017**, *69*, 88−99.

(53) Hensel, R. C.; Goncalves, M. H.; Rodrigues, K. L.; Oiko, V. T.; Pimentel, V. d. L.; Pereira-da-Silva, M. A.; Hillenkamp, M.; Riul, A., Jr; Rodrigues, V. Monitoring and modeling the deposition of metal nanoparticles on surfaces by impedance. *Appl. Surf. Sci.* **2021**, *544*, 148806.